OPEN ACCESS

KING'S College LONDON

King's Research Portal

DOI:
10.1109/ICRA.2018.8460921

Document Version
Early version, also known as pre-print

Link to publication record in King's Research Portal

Citation for published version (APA):
Mablekos-Alexiou, A., Ourselin, S., Cruz, L., & Bergeles, C. (2018). Requirements based design and end-to-end dynamic modeling of a robotic tool for vitreoretinal surgery. In *IEEE Int. Conf. Robotics and Automation* https://doi.org/10.1109/ICRA.2018.8460921

**Citing this paper**
Please note that where the full-text provided on King's Research Portal is the Author Accepted Manuscript or Post-Print version this may differ from the final Published version. If citing, it is advised that you check and use the publisher's definitive version for pagination, volume/issue, and date of publication details. And where the final published version is provided on the Research Portal, if citing you are again advised to check the publisher's website for any subsequent corrections.

**General rights**
Copyright and moral rights for the publications made accessible in the Research Portal are retained by the authors and/or other copyright owners and it is a condition of accessing publications that users recognize and abide by the legal requirements associated with these rights.

•Users may download and print one copy of any publication from the Research Portal for the purpose of private study or research.
•You may not further distribute the material or use it for any profit-making activity or commercial gain
•You may freely distribute the URL identifying the publication in the Research Portal

**Take down policy**
If you believe that this document breaches copyright please contact librarypure@kcl.ac.uk providing details, and we will remove access to the work immediately and investigate your claim.

Download date: 06. May. 2023

# Requirements Based Design and End-to-End Dynamic Modeling of a Robotic Tool for Vitreoretinal Surgery

Anestis Mablekos-Alexiou, Sebastien Ourselin, Lyndon da Cruz*, and Christos Bergeles*

***Abstract*— Despite several robots having been proposed for vitreoretinal surgery, there is limited information on their dynamic modeling. This gap leads to sub-optimal motor selection and hinders the application of advanced control schemes that would fulfill the goal of micro-precise surgery. This paper presents the design process and a dynamics study of a multi-Degree of Freedom (DoF) robotic system, which is inspired by established co-manipulation architectures. A rigorous kinematics and dynamics analysis of the robot's part that is responsible for manipulating the surgical tool during the retinal surgery phase is provided. In particular, the Euler-Lagrange equations of motion, which describe the dynamics of the 3-link surgical manipulator, are combined with novel analytical models of each link's corresponding transmission mechanism, including an anti-backlash lead screw assembly and a worm drive. The resulting models, transferable to existing manipulators, provide a meticulous analysis of the robot's performance that can be used both for mechanical design and control purposes.**

## I. Introduction

Vitreoretinal surgery and the precise subretinal delivery of upcoming sight-restoring therapeutics necessitate micrometer level precision. The required degree of accuracy, combined with the restricted limits of human ability [1-3], suggest that tailored robotic systems can improve intervention outcomes.

Within only a few decades from its initial introduction, vitreoretinal robotic surgery has evolved into a dynamic and rapidly growing research area. Initially proposed for assisting surgeons in challenging but common tasks that require high dexterity, such as epiretinal membrane peeling, [4], [5], vitreoretinal robots are now involved in new treatment methods offering capabilities that together with emerging stem cell [6] and gene therapies are expected to revolutionize retinal microsurgery and fulfill the goal of sight regeneration.

Nowadays, the breadth of proposed vitreoretinal surgical platforms is impressive and the technological contributions from roboticists have driven the field to a high level of maturity [7-12]. Despite the undeniable progress in terms of design and control strategies, however, the daunting requirement of micrometer accuracy affects the whole design process and introduces several technical hurdles to be overcome. The control challenges that arise, in combination with the constraints that exist in the operating theater, so far hinder the clinical adoption of vitreoretinal robots, despite impressive first-in-human trials by [7], [8].

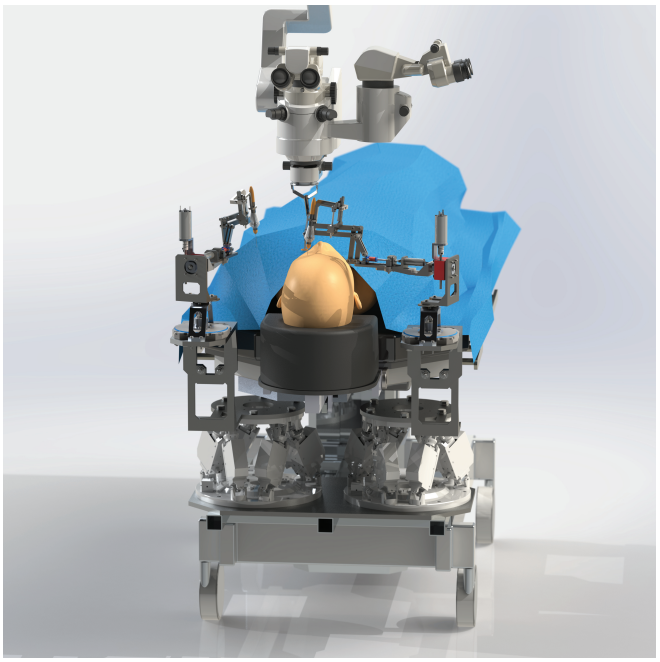

Fig. 1. Computer-Aided Design (CAD) model of the proposed robotic system installed in the surgical environment.

In this paper, we present a new design for a vitreoretinal surgery robot inspired by successful co-manipulation platforms [7], [11]. We consider the ergonomic and structural limitations in vitreoretinal surgery, and propose a coarse-to-fine surgical robot designed to minimize the disruption of the clinical workflow. We present a design process that is directed by the dynamics of the proposed manipulator. By combining the robot's equations of motion with novel mathematical models of its corresponding actuators, we obtain a detailed description of the robot's kinematics and dynamics. That description includes all the nonlinearities due to friction that arise from the use of transmission systems such as lead screws and worm gear drives, which are widely used in robotic microsurgery but rarely thoroughly investigated. The developed models can support the requirements-based selection of micro-actuators, allowing customized configurations that avoid off-the-shelf products that might affect the manipulator's precision and speed capabilities of the manipulator. Further, our approach

*Equal senior authorship.

This research was supported by the Michael Uren Foundation, Helena Charitable Trust, an ERC Starting Grant [714562], a UCL-Future Leaders Award, a Wellcome/EPSRC Centre of Excellence Award [203145Z/16/Z], and the EPSRC-funded UCL Centre for Doctoral Training in Medical Imaging [EP/L016478/1].

All authors are with the Wellcome/EPSRC Centre for Interventional and Surgical Sciences, UCL, London, UK. Anestis Mablekos-Alexiou and Lyndon da Cruz are additionally with UCL Institute of Ophthalmology and Moorfields Eye Hospital, London, UK. Sebastien Ourselin and Christos Bergeles are additionally with the Centre for Medical Image Computing, UCL, London, UK (corresponding author Anestis Mablekos-Alexiou, e-mail: anestis.mamplekos-alexiou.16@ucl.ac.uk or mamplekos@gmail.com).

supports the future introduction of accurate control strategies that include the system's dynamics.

The proposed robotic setup is illustrated in Fig. 1. The requirements driving its design are given in Sec. II, while Sec. III derives the dynamics of the 3-DoF end-effector. Section IV presents the models of the transmission mechanisms, while Sec. V describes the dynamics-informed selection of motors. The paper concludes in Sec. VI.

## II. Robotic System Design

Since successful clinical adoption requires minimal disruption to the ordinary clinical procedures, the developed robotic mechanism is designed to exploit the available free space in the operating room. Real surgery conditions and space arrangement of key components have been replicated using Computer-Aided Design (CAD) software, designing, from scratch, the operating table (Opmaster 506P from Lab-Med) and surgical microscope (Lumera 700 from Zeiss), see Fig. 1. This way, the robotic mechanism can be designed to fit in the available space. The system's mechanical design begins by analysing tool movement during conventional vitreoretinal surgery, and mapping the motions to the robot components responsible for their execution.

### A. Introduction to Design Goals

Each operation can be divided into three tool-motion phases [12]: the approach phase (A-phase), the insertion phase (I-phase), and the retinal surgery phase (S-phase).

The A-phase corresponds to the stage where the surgeon brings the tool from a random initial position to the incision point on the eye surface. Usually, there are three incision points, fitted with trocars: one for the surgical tool, one for the endoillumination probe, and one for an infusion line to keep the intraocular pressure constant. A-phase motion corresponds to a typical translation in space, and, consequently, requires a robot with at least three DoF.

The I-phase includes the motion of the tool tip starting from the incision until the retinal surface, while the S-phase includes all motions of the tool into the eye chamber rotating about the entrance at the incision point. Concerning the I- and S-phase, three rotational DoF around a Remote Center of Motion (RCM) and one translational that passes through it are kinematically needed to achieve pivoting on the RCM and tool insertion/retraction.

A robotic system that fulfills the requirements of vitreoretinal surgery can be divided into two independent "sub-robots"; a coarse manipulator and a fine manipulator. The first, the A-Robot, is responsible for positioning the RCM during the A-phase. The second, termed S-Robot, is responsible for the S-phase execution (I-phase is a subset of it), and corresponds to the part that interacts with both surgeon and patient and requires the high-quality design.

### B. Design of A-Robot

A mechanism that provides at least three translational DoF with a sufficient range of motion is suitable for the A-phase. In this work, an off-the-shelf 6-DoF hexapod-based assembly (H-825 from Physik Instrumente), compact enough to fit under the surgical table, is selected for transferring the RCM to the desired incision point. Custom flanges are designed to connect the S-Robot with the hexapod and place it at a position next to the table's pillow, see Fig. 1. We include an additional rotating component that functions as the base for the S-Robot, adding an extra rotational DoF, see Fig. 2. This unconstrained rotation, provided by an off-the-shelf low profile stage (U-651 from PI), offers the option of moving the robot away from the working area at a position that does not cause disruption to the workflow when not used. Both manipulators are self-locking when switched off, and positioning accuracy is not affected by external disturbances; the energy dissipated by holding the tool during surgery is minimized. The A-Robot's positioning specifications are given in Table I.

TABLE I
A-Robot Positioning Specifications

| Motion and Positioning Specifications | Units | Value |
|---|---|---|
| Travel range in XY | $mm$ | 60 |
| Travel range in Z | $mm$ | 35 |
| Rotation range about X, Y, Z | $\circ$ | 30 |
| Repeatability in X, Y, Z | $\mu m$ | 0.5 |

### C. Design of S-Robot

The S-Robot consists of a roll and a tilt mechanism whose axes of rotation intersect at a specific point in space providing a mechanical RCM, similar to [7], [11]. An insertion component is attached on the tip of the tilt mechanism and provides an additional translational DoF, responsible for driving the tool in and out of the eye chamber, passing through the RCM, see Fig. 3.

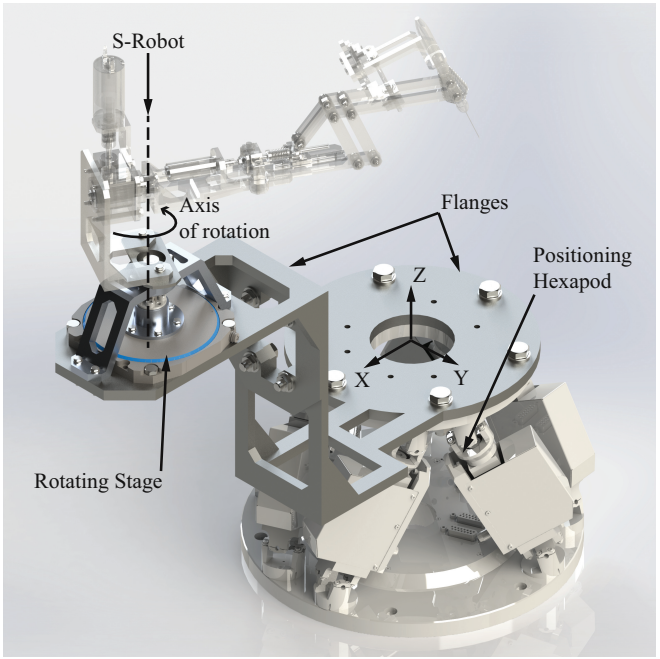


Fig. 2. Illustration of the A-Robot subassembly, consisting of a 6-DoF positioning hexapod and a low profile rotating stage.

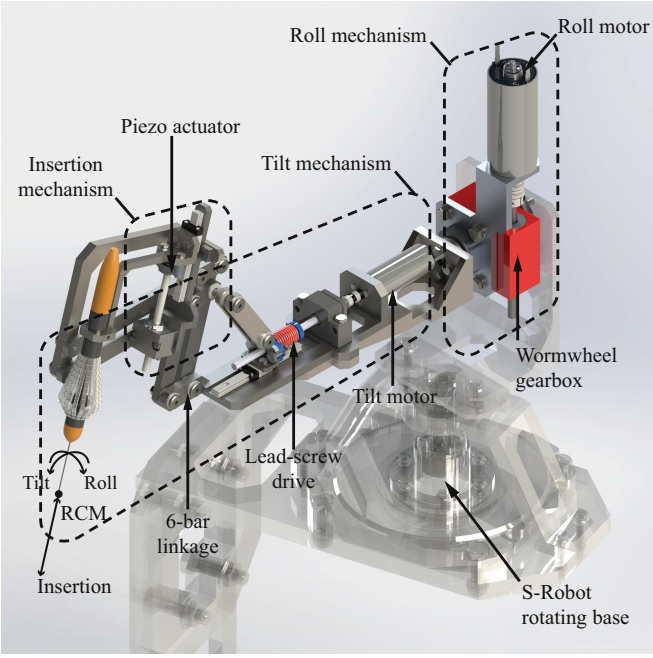


Fig. 3. Illustration of S-Robot subassembly, consisting of a roll, tilt, and an insertion component.

The insertion assembly employs an off-the-shelf piezo actuator (N-422 from PI), due to its accuracy and compactness. The actuator provides continuous motion with 35mm travel range, 30mm/s maximum velocity and a step size at around 300nm.

A wormwheel based configuration is designed to produce roll motion. The components that constitute this mechanism are a wormwheel gearbox (P20-120AR from Ondrives), a custom designed rotating shaft that transfers the power to all rotating components, and an actuating motor. The range of motion provided by the roll mechanism is 360°.

Concerning the tilt motion, a six-bar mechanism that provides a mechanical RCM is selected [13]. The six-bar linkage is actuated by a motorized lead screw drive (AFA016048RS from Helix). As the application requires extreme precision, an anti-backlash nut is chosen to eliminate the clearance caused by gaps between screw and nut. The provided range of tilt rotation about the RCM is around 60°.

The specifications of both roll and tilt motors are presented in Sec. V after estimation of the power that they must deliver.

## III. S-Robot Kinematics & Dynamics

The part of the robot that actively interacts with the patient and merits of deeper analysis is the S-Robot. Considering that the A-Robot is used for pre-positioning the RCM at the desired point, the two subassemblies can be studied separately as they are dynamically uncoupled.

### A. Forward Kinematics

In this section forward kinematics of the S-Robot manipulator are briefly developed, primarily to aid next subsection's dynamic modeling. For the derivation of the robot's homogeneous transformation matrices, the Denavit-Hartenberg (DH) convention is used.

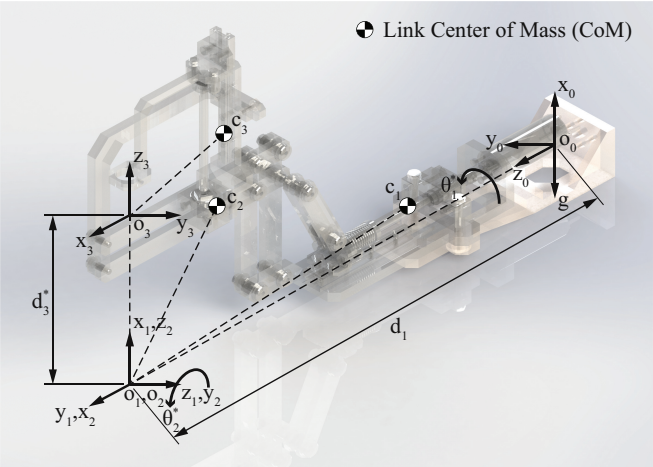


Fig. 4. Denavit-Hartenberg frame assignment for the 3-link S-Robot.

TABLE II
DH Parameters of the S-Robot

| Robot Link | DH Parameters | | | |
|---|---|---|---|---|
| | $a_i$ | $\alpha_i$ | $d_i$ | $\theta_i$ |
| 1 | 0 | $\pi/2$ | $d_1$=0.28m | $\theta_1^*$ |
| 2 | 0 | $\pi/2$ | 0 | $\theta_2^* + \pi/2$ |
| 3 | 0 | 0 | $d_3^*$ | 0 |

The coordinate frame assignment in space is illustrated in Fig. 4, where $o_0x_0y_0z_0$ is the selected inertial base frame, and is chosen to be placed on the roll axis of rotation at the point of connection with the corresponding transmission system. Once the base frame is established, the $o_1x_1y_1z_1$ frame is fixed at the mechanical RCM point at a distance $d_1$ from $o_0$, and is rotated about the $z_0$-axis. This angle of rotation is a joint variable and is denoted by $\theta_1$. Subsequently, the $o_2x_2y_2z_2$ frame is also fixed at the RCM and can rotate about the $z_1$-axis at a variable tilt angle, which is denoted by $\theta_2$. The last frame $o_3x_3y_3z_3$ is placed at the point of the tool tip whose position is controlled. The origin $o_3$ is allowed translation at a variable distance $d_3$ along the $z_2$-axis. Finally, each vector $c_i = \begin{bmatrix} c_{xi} & c_{yi} & c_{zi} \end{bmatrix}^T$ denotes the position of the Center of Mass (CoM) of the $i$-th link expressed at the corresponding origin $o_i$. Consequently, based on the described frame assignment, the resulting DH parameters $\theta_i$, $d_i$, $a_i$, $\alpha_i$ are written in Table II.

The forward kinematics equations are obtained using the four quantities of the DH convention given in Table II and substituting them into the homogeneous transformation matrices $A_i$ for each link given by [14].

Subsequently, using the time derivatives of the resulting rotation matrices $R \in SO(3)$ and the assigned coordinate frame, three manipulator Jacobians are derived. The derived expressions of the above functions for this particular manipulator are straightforward and are omitted for brevity.

### B. Dynamics

The Euler-Lagrange equations of motion (EoM) are used to describe the dynamic behavior of the S-Robot. For the derivation of the manipulator's dynamic equations, its joint

variables are chosen as generalized coordinates. Therefore, $q = \begin{bmatrix} q_1 & q_2 & q_3 \end{bmatrix}^T$, where $q_1 = \theta_1$, $q_2 = \theta_2$, $q_3 = d_3$. The EoM for the $k$-th link can be written as

$$\sum_{j=1}^{3} d_{kj}(q)\ddot{q}_j + \sum_{i=1}^{3}\sum_{j=1}^{3} c_{ijk}(q)\dot{q}_i\dot{q}_j + g_k = \tau_k \qquad (1)$$

where $d_{kj}$ is the $(k,j)^{th}$ element of an inertia type matrix $D(q)$, $c_{ijk}$ are the Christoffel symbols, $g_k$ represents the effect of gravitational forces, and $\tau_k$ includes all the non-conservative torques applied on the link.

## IV. Modeling Of Transmission Mechanisms

The equations given by (1) describe the dynamic behavior of robot's links assuming that they freely rotate or translate along their corresponding axes. In most applications, however, between each actuator-link pair, a transmission system is responsible for transferring appropriately the mechanical power. In a vitreoretinal surgical robot, where precision requirements are extremely high, detailed modeling of the transmission systems is important in terms of both achieving satisfactory control, and accurate power estimation for design purposes, since the intense friction phenomena affect both of these factors. In this particular study, the designed roll and tilt actuators include a wormwheel mechanism and an anti-backlash lead screw drive, which are both widely used in robotic positioning applications. These transmission models have not so far been included in the context of the dynamics of micro-precise robots, and are developed from scratch.

### A. Wormwheel Gearbox

Power transmission for the roll mechanism is implemented with a wormwheel gearbox. The actuating motor is connected to the worm-shaft and transmits power to all rotating components of the assembly attached on the gear. Therefore, this system consists of two rigid bodies, which are kinematically coupled, and consequently one EoM fully describes its dynamics.

The dynamic equations of each of the two components are analyzed sequentially. First, the worm-shaft EoM, which is directly connected to the motor, may be written as

$$J_w\ddot{\theta}_w = \tau_w + \tau_w^{'} \qquad (2)$$

where $\theta_w$ is the worm angle, $J_w$ the worm-shaft inertia, $\tau_w$ the torque generated by the actuating motor, and $\tau_w^{'}$ the torque on the shaft due to the interaction with the gear.

Concerning the rotating gear, which is directly connected with the link-1 of the manipulator, its dynamics are given by (1) for $k = 1$. To relate this expression with the worm-shaft dynamics, (1) is reformulated as

$$d_{11}(q)\ddot{q}_1 = \tau_1^{'} + \tau_g^{'} - \sum_{j=2}^{3} d_{1j}(q)\ddot{q}_j - \sum_{i=1}^{3}\sum_{j=1}^{3} c_{ij1}(q)\dot{q}_i\dot{q}_j - g_1 \qquad (3)$$

where the inertial term $d_{11}(q)\ddot{q}_1$ that contains the gear's acceleration is separated from the remaining equation, $\tau_1^{'}$ denotes the sum of non-conservative torques excluding the $\tau_g^{'}$ torque which is generated due to the interaction with the worm-shaft. Equation (3), then, can be written as

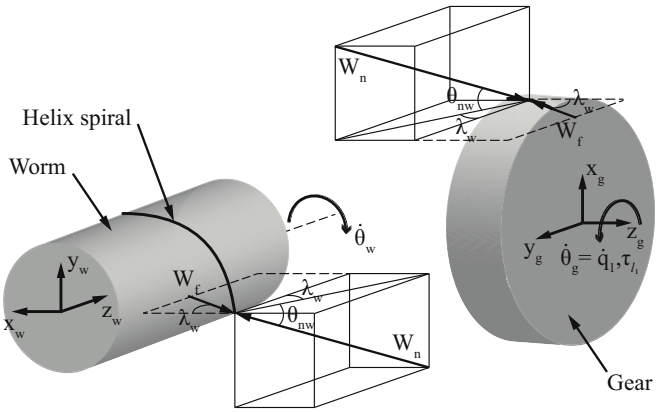


Fig. 5. Free body diagrams of the worm gear transmission system for positive gear angular velocity and external torque.

$$d_{11}(q)\ddot{q}_1 = \tau_{l_1} + \tau_g^{'} \qquad (4)$$

where

$$\tau_{l_1} = \tau_1^{'} - \sum_{j=2}^{3} d_{1j}(q)\ddot{q}_j - \sum_{i=1}^{3}\sum_{j=1}^{3} c_{ij1}(q)\dot{q}_i\dot{q}_j - g_1. \qquad (5)$$

We then combine (2) and (4) to identify the relation of torques $\tau_w^{'}$, $\tau_g^{'}$. For that purpose, the free body diagrams of the worm and gear are depicted in Fig. 5. It is noted that these forces' analysis is valid when both the gears velocity $\dot{q}_1$ and external torque $\tau_{l_1}$ are positive based on the body-attached coordinate frames and for the selected right-hand worm helix. In Fig. 5, $\lambda_w$ denotes the worm's lead angle, $\theta_{nw}$ the spiral's pressure angle, $d_w$ the worm's diameter, $d_g$ the gear's diameter, $W_f$ the frictional forces between the sliding surfaces and $W_n$ the normal to pitch helix forces, as defined by the theory of machine elements [15]. Identifying the forces that generate torques at the direction of motion, the expressions for the torques $\tau_g^{'}$ and $\tau_w^{'}$ are

$$\tau_g^{'} = \frac{d_g}{2}(W_n \cos\theta_{nw}\cos\lambda_w + W_f \sin\lambda_w) \qquad (6)$$

$$\tau_w^{'} = \frac{d_w}{2}(W_f \cos\lambda_w - W_n \cos\theta_{nw}\sin\lambda_w). \qquad (7)$$

Assuming that the coefficient of friction is constant across the length of the spiral then

$$W_f = \mu W_n. \qquad (8)$$

Substituting (8) into (6), (7), and eliminating the internal forces $W_n$ by combining (2) and (4), the following dynamics expression is obtained

$$J_w\ddot{\theta}_w - \xi_{w_1}\frac{d_w}{d_g}\ddot{q}_1 = \tau_w - \xi_{w_1}\frac{d_w}{d_g}\tau_{l_1} \qquad (9)$$

where

$$\xi_{w_1} = \frac{\mu\cos\lambda_w - \cos\theta_{nw}\sin\lambda_w}{\cos\theta_{nw}\cos\lambda_w + \mu\sin\lambda_w} \qquad (10)$$

is a function of both worm-shaft geometry as well as coefficient of friction $\mu$ and can be positive or negative

determining the backdrivability of the transmission system. It is noted that any model of friction might be used for describing the solid-to-solid contact of sliding surfaces by using the corresponding coefficient model.

The kinematic equation that relates worm and gear angular positions is positive for the selected coordinate frames and is calculated by

$$\theta_w = q_1 n_w \tag{11}$$

where $n_w$ is the transmission's reduction ratio.

Substituting (11) into (9) the dynamics equation of the manipulator as seen by the roll motor side is

$$(J_w - \xi_{w_1} \frac{1}{n_w} \frac{d_w}{d_g} d_{11}) \ddot{\theta}_w = \tau_w - \xi_{w_1} \frac{d_w}{d_g} \tau_{l_1}. \tag{12}$$

As mentioned, the above expression occurs when the external gear torque $\tau_w$ and worm-gear velocities $\dot{\theta}_w$, $\dot{q}_1$ are positive. As revealed by (12), for positive $\xi_{w_1}$, the external torque decelerates the system, although it is acting on the direction of velocity. In that case the transmission is non-backdrivable and any external torque applied on the rotating component increases the system's friction.

Performing the same analysis for all the possible torque-velocity direction combinations as well as for the case of a left-hand worm helix, and generalizing the analysis for the $k$-th link of a manipulator, it turns out that the only information needed to fully define link's EoM, when driven by a worm gear, is the sign of the product of link's velocity $\dot{q}_k$ multiplied by the total external load $\tau_{l_k}$ applied on it. For simplification of the final dynamics expression, we define

$$J_{w_{1,2}} = \mp \xi_{w_{1,2}} \frac{1}{n_w} \frac{d_w}{d_g} d_{kk} \tag{13}$$

$$C_{w_{1,2}} = \pm \xi_{w_{1,2}} \frac{d_w}{d_g} d_{kk} \tag{14}$$

where $d_{kk}$ represents the moment of inertia at joint-$k$ axis, when the other joints are blocked, as revealed by (1). Furthermore, $\xi_{w_1}$ is given by (10) and $\xi_{w_2}$ is

$$\xi_{w_2} = \frac{\mu \cos\lambda_w + \cos\theta_{nw} \sin\lambda_w}{\cos\theta_{nw} \cos\lambda_w - \mu \sin\lambda_w}. \tag{15}$$

Therefore, the EoM of a robot's $k$-th link that is driven by a wormwheel transmission, as seen by the actuating motor, may be written as follows

$$(J_w + J) \ddot{\theta}_w = \tau_w - C \tau_{l_k} \tag{16}$$

where

- If $\tau_{l_k} \dot{q}_k > 0$: $J = J_{w_1}$ and $C = C_{w_1}$
- If $\tau_{l_k} \dot{q}_k < 0$: $J = J_{w_2}$ and $C = C_{w_2}$
- If $\tau_{l_k} = 0$: $J = J_{w_2}$ and $C = C_{w_2}$

It is noted that $\tau_{l_k}$ is calculated by reformulating (5) for the case of the $k$-th link of an $n$-link manipulator. Equation (16) is a generalization of the equations derived from the analysis of all rotation cases, and can be used for any coordinate system, or any direction of external loads. The only information needed is the geometrical characteristics of the worm gear assembly, as well as the friction coefficient between the sliding surfaces.

### *B. Anti-backlash Lead Screw Assembly*

The tilt mechanism consists of an actuating motor, an anti-backlash lead screw drive, and a 6-bar linkage. The Euler-Lagrange EoM of this particular link of the robot is given from (1) for $k = 2$. Reformulating the resulting expression as with the case of the roll component, the dynamics may be written as

$$d_{22}(q) \ddot{q}_2 = \tau_{l_2} + \tau_n^{'} \tag{17}$$

where $\tau_n^{'}$ denotes the torque produced by the pushing nut of the lead screw, and $\tau_{l_2}$ includes the remaining non-conservative torques as well as the centrifugal and Coriolis terms, and is given by (5) for $k = 2$. In order to relate the above dynamic expression with the nut of the lead screw, which moves linearly, a velocity relationship between the link's rotation and nut's translation is needed. Here, that relation is given by the 6-bar linkage, which can be kinematically regarded as a standard crank mechanism.

Substituting the crank's kinematics into (17) yields the linear motion equation of the following form

$$m_{22}(q) \ddot{x}_2 = F_{l_2} + F_n^{'}. \tag{18}$$

Equation (18), therefore, describes the dynamics of the link as seen by the linearly moving part of it, which corresponds to the nut. An anti-backlash nut, however, consists of two distinct parts, with masses $m_1$ and $m_2$, respectively. Establishing the convention that the link is connected with the $m_2$-part, then the dynamic model of the body, which consists of the corresponding robot link and the $m_2$-part of the nut, is described by (18).

The expressions for the remaining parts of the lead screw are derived from the corresponding free body diagrams. For this type of transmission, the forces' analysis is derived by extending a screw spiral with its nut along a surface [16]. The resulting schematic representation is shown in Fig. 6. The positive directions for nut and screw velocities $\dot{x}_2$, and $\dot{\theta}_s$, respectively, are indicated. The screw inertia is denoted by $J_s$, the screw diameter by $d_s$, the lead-angle by $\lambda_s$, the spiral pressure angle by $\theta_{ns}$, and the lead pitch by $p$. To facilitate the analysis, we write the external force $F_{l_2}$, as

$$F_{l_2} = F_{l_2}^{+} + F_{l_2}^{-}. \tag{19}$$

If $F_{l_2}$ is positive then $F_{l_2}^{-}$ equals zero, and respectively, if $F_{l_2}$ is negative $F_{l_2}^{+}$ is zero. In this way, we concurrently examine the effect of both direction external forces on the system. Using the above conventions, there are two cases of motion based on the direction of nut's velocity $\dot{x}_2$, which can be either positive (towards the direction of $m_2$) or negative (towards the direction of $m_1$).

The forces' analysis for positive $\dot{x}_2$ is depicted in Fig. 6, where $F_{fs_1}$ and $F_{fs_2}$ denote the frictional forces between the sliding surfaces of screw and nut, $F_{fn}$ the frictional force between the moving nut and the linear guide, $N_1 \cos\theta_{ns}$ and $N_2 \cos\theta_{ns}$ the normal to the pitch helix forces, $P$ the preloading spring force, and $\tau_s$ the motor torque. The force $F_{l_2}^{+}$ is only applied on the $m_2$-part, while on the other

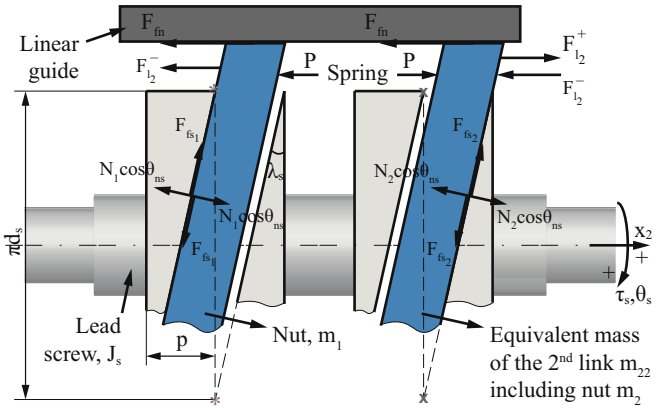


Fig. 6. Surface extended screw spiral and anti-backlash nut.

hand, $F_{l_2}^-$ on both nut parts as it is transmitted through the preloading spring from $m_2$ to $m_1$. Finally, the illustrated forces' analysis is valid only when the external $F_{l_2}^-$ load does not compress the spring. This can be ensured by estimating its extreme values for a specific application and selecting a sufficiently stiff preloading spring. In this case, the kinematic relation between screw and both parts of the nut is

$$x_2 = \tan\lambda_s \frac{d_s}{2}\theta_s. \tag{20}$$

Following the same procedure as with the case of the wormwheel drive, namely eliminating the internal forces $N_1$ and $N_2$, the final dynamics equation is obtained, and can be generalized for the random linearly moving $k$-th link of a robot, with equivalent mass $m_{kk}$ and driven by an anti-backlash lead screw transmission. Defining the following coefficients

$$J_{s_{1,2}} = \frac{d_s^2}{4}\tan\lambda_s(\psi_2 m_{1,kk} - \psi_1 m_{kk,1}) \tag{21}$$

$$C_{g_{1,2}} = \pm\frac{d_s}{2}\psi_{1,2} \tag{22}$$

where

$$\psi_{1,2} = \frac{\mu\cos\lambda_s \mp \cos\theta_{ns}\sin\lambda_s}{\cos\theta_{ns}\cos\lambda_s \pm \mu\sin\lambda_s} \tag{23}$$

the EoM of the $k$-link driven by an anti-backlash lead screw drive, as seen by the actuating motor's ouput shaft, may be written as follows

$$(J_s + J)\ddot{\theta}_s = \tau_s - \tau_f - C^- F_{l_k}^- - C^+ F_{l_k}^+ \tag{24}$$

where

$$\tau_f = \frac{d_s}{2}[P(\psi_2 + \psi_1) + F_{fn}(\psi_2 - \psi_1)]\,\mathrm{sgn}\,\dot{\theta}_s \tag{25}$$

$$C^- = \frac{d_s}{2}(\psi_2 - \psi_1) \tag{26}$$

and

- If $\dot{x}_k$ is in the direction of $m_2$: $J = J_{s_1}$ and $C^+ = C_{g_1}$
- If $\dot{x}_k$ is in the direction of $m_1$: $J = J_{s_2}$ and $C^+ = C_{g_2}$

The above expression can be used for any anti-backlash lead screw drive, where the EoM of the link that is attached on the $m_2$-part of the nut is of the form given by (18).

## V. Power Considerations and Motorization

The end-to-end dynamic modeling of the robotic manipulator provides the ability of accurate estimation of power demands based on given performance specifications.

We set up the requirements as a motion response that contains the maximum angular and linear velocities that the robot must achieve, as simulated in Fig. 7 for a time interval of $15s$. We are mainly focusing on the roll and tilt components that we plan to motorize simulating extreme for the application velocity responses. The simulated interval shown in Fig. 7 depicts the velocity response of the two rotational components, containing an impulse-like phase $(0 - 2.5s)$ and a sinusoidal one $(2.5 - 15s)$ of three different frequencies; namely $2Hz$, $1Hz$, and $0.5Hz$. The maximum values of acceleration $\ddot{q}_{1,2}$, and velocity $\dot{q}_{1,2}$ are at around $200°/s^2$ and $65°/s$, respectively. Both maximum values as well as sinusoidal frequencies are retrieved from literature [1], [17]. Although, a motorization procedure is not required for the insertion component as its actuation is already selected, its motion affects the dynamics of the system as revealed by (1). Therefore, a motion with the maximum velocity that the actuator produces is simulated at the same time interval, see Fig. 7.

After expressing the requirements for the S-Robot and using the corresponding kinematic relations, the motion that each motor-shaft must follow is obtained. Subsequently, using (16) and (24), depending on the transmission type, and solving for $\tau_w$ and $\tau_s$, respectively, the amount of each motor torque needed to produce the simulated motion is obtained, together with a power consumption estimation.

For the motorization procedure, it is useful to obtain an expression of the required motor torque with respect to the corresponding velocity. The reason is that each motor's function is affected by its operating range which determines the limits of its continuous operation in terms of the output torque and velocity. Based on the motion requirements given in Fig. 7 and the transmission models that have been developed in this paper, the resulting torque-velocity $(\tau - \omega)$ curves for both roll and tilt motors are presented in Fig. 8, using the parameters in Table III, IV.

For the motor selection, it is important to highlight that in this particular application the use of a gearbox at the motors' output is avoided due to the backlash that it introduces. Therefore, the torque load, calculated for each motor in Fig. 8, has to be directly in its operating range. Consequently, the most critical point to identify from the simulation results is the maximum absolute values of torque that appear in the resulting $(\tau - \omega)$ curves. In particular, the maximum values are slightly less than $10mNm$ for both links. Thus, a motor with nominal torque at $10mNm$ or higher is considered suitable. Our design is finalized by selecting the DCX-16L DC Motor from Maxon Motor AG with nominal torque at $12mNm$, for both roll and tilt links.

It is noted that the Static-plus-Kinetic friction model has been used with $\mu_{st} = 0.15$, and $\mu_{kin} = 0.11$ the static and kinetic friction coefficients, respectively.

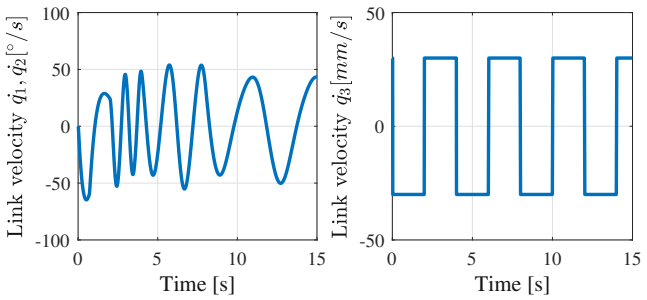


Fig. 7. S-Robot velocity specifications: Velocity response of rotational links 1-2 (left), Velocity response of translational link (right).

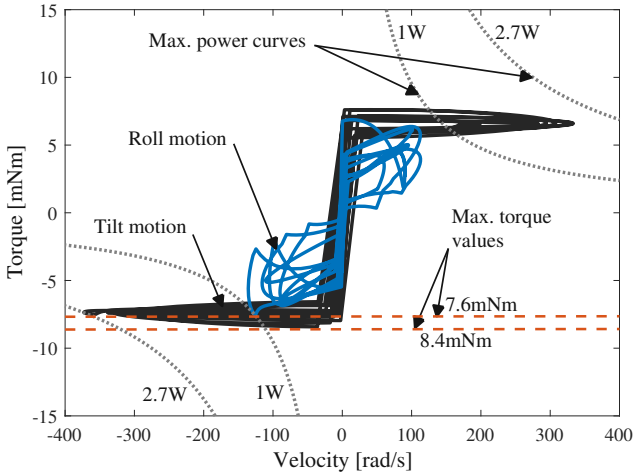


Fig. 8. Torque-velocity load curves: Roll motion (blue), Tilt motion (black).

Through the presented kinematics and dynamics process, the optimal robot for the required motion models can be selected, keeping the dimensions of the system optimal and its behavior within the range of what retinal surgery requires.

## VI. Conclusion

This paper presented our design considerations for a micro-precise robot for vitreoretinal surgery, with the ultimate goal of subretinal therapeutics delivery. Our primary contribution is the end-to-end development of the manipulator's dynamics equations, and the demonstration of a design process that uses the said equations to motorize the system. Our future work entails synthesis of a model-based controller, and engineering of the S-Robot for experimentation.

TABLE III

Transmission Parameters

| **Parameters [SI]** | | **Transmission Type** | |
|---|---|---|---|
| ***Name*** | ***Symbol*** | ***Worm drive*** | ***Lead screw*** |
| Lead angle | $\lambda$ | $1.34\pi/180$ | $7.8\pi/180$ |
| Pressure angle | $\theta_n$ | $30\pi/180$ | $30\pi/180$ |
| Inertia | $J$ | $4.5e-7$ | $5e-7$ |
| Nut mass | $m_1$ | – | 0.02 |
| | $m_2$ | – | 0.02 |
| Diameter | $d_w$ | $11e-3$ | – |
| | $d_g$ | $31e-3$ | – |
| | $d_s$ | – | $3.175e-3$ |
| Reduction ratio | $n_w$ | $120:1$ | – |

TABLE IV

S-Robot Parameters

| **Robot Link** | **Parameters [SI]** | | |
|---|---|---|---|
| | ***Mass*** | ***Inertial Tensor*** | ***Center of Mass*** |
| Link 1 | 0.568 | $10^{-3}\begin{bmatrix}1.34 & 0.12 & 0.00\\ 0.12 & 0.12 & 0.00\\ 0.00 & 0.00 & 1.36\end{bmatrix}$ | $\begin{bmatrix}0.002\\ -0.196\\ 0.00\end{bmatrix}$ |
| Link 2 | 0.166 | $10^{-3}\begin{bmatrix}0.19 & 0.00 & 0.11\\ 0.00 & 0.43 & 0.00\\ 0.11 & 0.00 & 0.25\end{bmatrix}$ | $\begin{bmatrix}-0.055\\ -0.015\\ 0.069\end{bmatrix}$ |
| Link 3 | 0.145 | $10^{-3}\begin{bmatrix}0.10 & 0.00 & 0.00\\ 0.00 & 0.15 & 0.00\\ 0.00 & 0.00 & 0.06\end{bmatrix}$ | $\begin{bmatrix}0.00\\ 0.00\\ 0.106\end{bmatrix}$ |

## References


[1] L. F. Hotraphinyo and C. N. Riviere, "Three-dimensional accuracy assessment of eye surgeons," *IEEE Int. Conf. Engineering in Medicine and Biology Soc.*, vol. 4., pp. 3458-3461, 2001.

[2] A. D. Jagtap and C. N. Riviere, "Applied Force during Vitreoretinal Microsurgery with Handheld Instruments," *IEEE Int. Conf. Engineering in Medicine and Biology Soc.*, pp. 2771-2773, 2004.

[3] S. P. N. Singh and C. N. Riviere, "Physiological Tremor Amplitude during Retinal Microsurgery," *IEEE Northeast Bioengineering Conference*, Philadelphia, pp. 171-172, 2002.

[4] C. N. Riviere, W. T. Ang, and P. K. Khosla, "Toward active tremor canceling in handheld microsurgical instruments," *IEEE Trans. Robotics and Automation*, vol. 19, no. 5, pp. 793-800, 2003.

[5] R. Taylor et al., "A Steady-Hand Robotic System for Microsurgical Augmentation," *Int. Journal of Robotics Research*, vol. 18, no. 12, pp. 1201-1210, 1999.

[6] C. M. Ramsden, M. B. Powner, A. J. Carr, M. J. Smart, L. da Cruz, and P. J. Coffey (2013). Stem cells in retinal regeneration: past, present and future. Development (Cambridge, England), 140(12), 257685.

[7] A. Gijbels, E. B. Vander Poorten, P. Stalmans, H. Van Brussel, and D. Reynaerts, "Design of a Teleoperated Robotic System for Retinal Surgery," *IEEE Int. Conf. Robotics and Automation*, pp. 2357-2363, 2014.

[8] H. Meenink et al., "Robot-assisted vitreoretinal surgery," *Medical Robotics: Minimally Invasive Surgery*, pp. 185-209, 2012.

[9] M. Nambi, P. S. Bernstein, and J. J. Abbott, "A Compact Telemanipulated Retinal-Surgery System that Uses Commercially Available Instruments with a Quick-Change Adapter," *Journal of Medical Robotics Research*, vol. 1, no. 2, 2016.

[10] M.A. Nasseri, "Hybrid Parallel-Serial Micromanipulator for Assisting Opthalmic Surgery," Ph.D. dissertation, TUM, Munich, 2014.

[11] A. Uneri et al., "New Steady-Hand Eye Robot with Micro-Force Sensing for Vitreoretinal Surgery," *Int. Conf. Biomedical Robotics and Biomechatronics*, pp. 814-819, 2010.

[12] B. Mitchell et al., "Development and Application of a New Steady-Hand Manipulator for Retinal Surgery," *IEEE Int. Conf. Robotics and Automation*, pp. 623-629, 2007.

[13] R. H. Taylor, J. Fund, D. D. Grossman, J. P. Karidis, and D. A. LaRose, "Remote center-of-motion for surgery," US Patent 5,397,323, March 14, 1995.

[14] J. Denavit and R.S. Hartenberg, "A kinematic notation for lower pair mechanisms based on matrices," *Trans. American Society of Mechanical Engineers (ASME). Journal of Applied Mechanics*, vol. 77, pp. 215-221, 1995.

[15] G. Budynas Richard and Nisbett J. Keith, *Shigley's Mechanical Engineering Design*, New York, United States of America: McGraw-Hill Education, 2015.

[16] A. Mablekos-Alexiou, G. A. Bertos, and E. Papadopoulos, "A Biomechatronic Extended Physiological Proprioception (EPP) Controller for Upper-Limb Prostheses," *IEEE/RSJ Int. Conf. Intelligent Robots and Systems*, pp. 6173-6178, 2015.

[17] M. A. Nasseri et al., "Kinematics and Dynamics Analysis of a Hybrid Parallel-Serial Micromanipulator Designed for Biomedical Applications," *IEEE/ASME Int. Conf. Advanced Intelligent Mechatronics*, pp. 293-299, 2013.